PAPER

Check for updates

Single-layer metal halides MX$_2$ (X = Cl, Br, I): stability and tunable magnetism from first principles and Monte Carlo simulations†

Vadym V. Kulish [iD] *[a] and Wei Huang*[b]

Based on first-principles calculations, we investigate a novel class of 2D materials – MX$_2$ metal dihalides (X = Cl, Br, I). Our results show that single-layer dihalides are energetically and dynamically stable and can be potentially exfoliated from their bulk layered forms. We found that 2D FeX$_2$, NiX$_2$, CoCl$_2$ and CoBr$_2$ monolayers are ferromagnetic (FM), while VX$_2$, CrX$_2$, MnX$_2$ and CoI$_2$ are antiferromagnetic (AFM). The magnetic properties of 2D dihalides originate from the competition between AFM direct nearest-neighbor d–d exchange and FM superexchange *via* halogen p states, which leads to a variety of magnetic states. The thermal dependence of magnetic properties and the Curie temperature of magnetic transition are evaluated using statistical Monte Carlo simulations based on the Ising model with classical Heisenberg Hamiltonian. The magnetic properties of single-layer dihalides can be further tuned by strain and carrier doping. Our study broadens the family of existing 2D materials with promising applications in nanospintronics.

1. Introduction

Tremendous research attention is currently focused on two-dimensional (2D) nanomaterials due to their rich physical properties and diverse technological applications.[1–3] The possibility of designing magnetic 2D nanostructures is particularly intriguing and can be useful for spintronics and nanoscale magnetic memory devices.[4] Most 2D nanomaterials, however, do not show any intrinsic magnetism with only rare exceptions.[5–13] The strategies to induce magnetic moments in otherwise non-magnetic 2D materials include defect engineering,[14] strain,[15] adatom adsorption,[16–22] and substitutional doping.[23,24] However, the resulting materials lack experimental controllability and stability. Moreover, metal dopants tend to form clusters due to strong d–d interactions resulting in non-homogenous magnetization and low Curie temperature values. Identifying magnetic 2D nanomaterials thus has been a challenge.

Here, we examine a novel class of 2D nanostructures – single-layer metal dihalides (MX$_2$, where X = Cl, Br, I). Surprisingly, this class of nanomaterials is relatively unexplored despite the presence of stable layered structures in the bulk. However, halides start

to attract research attention now, including the layered ones.[25–28] For instance, the experimentally synthesized layered BiI$_3$ has a bandgap of 1.8 eV and demonstrates room-temperature band-edge photoluminescence.[29–31] Layered ternary bismuth iodides show good photovoltaic performance with an extra advantage of the significantly reduced toxicity of Bi when compared with Pb.[32] Theoretical calculations demonstrate that single-layer PbI$_2$ is stable and exhibits interesting exciton and spin–orbit coupling effects.[33,34] Monolayer GaBiCl$_2$, ZrBr and HfCl were identified as room-temperature quantum spin Hall insulators with large nontrivial band gaps.[35,36] FeCl$_2$ displays a half-metallic ferromagnetic ground state.[37,38] Recent experimental studies demonstrated that single crystals of CrI$_3$ can be cleaved very easily, possess a ferromagnetic order even in the monolayer form, and are stable in air/water, in the absence of CrI$_2$ contamination.[39–41] The above studies show a high potential of 2D halides from both fundamental and applied perspectives.

In this work, we demonstrate that single-layer metal dihalides are energetically stable and possess intrinsic ferromagnetism. Their magnetic properties originate from the competition between antiferromagnetic (AFM) direct nearest-neighbor d–d exchange and ferromagnetic (FM) superexchange *via* halogen p states, leading to a variety of magnetic states. By using density functional theory (DFT) methods, we determine the ground-state magnetic ordering and calculate the exchange coupling constants in 2D dihalides. The thermal dependence of magnetic properties and the Curie temperature of magnetic transition are

[a] Department of Mechanical Engineering, National University of Singapore, 21 Lower Kent Ridge Rd, 119077, Singapore. E-mail: kulishvadym@gmail.com

[b] Institute of Systems Science, National University of Singapore, 25 Heng Mui Keng Terrace, 119615, Singapore. E-mail: huangwei860921@gmail.com

† Electronic supplementary information (ESI) available: Phonon dispersions, stability and density of states for all dihalides. See DOI: 10.1039/c7tc02664a

8734 | *J. Mater. Chem. C*, 2017, **5**, 8734–8741

This journal is © The Royal Society of Chemistry 2017

estimated using statistical Monte Carlo (MC) simulations based on the Ising model. We find that single-layer dihalides exhibit comparable or even slightly higher Curie temperatures than single-layer dichalcogenides. This can be attributed to the profound ionic bonding in halides, which enhances the super-exchange coupling between the magnetic metal ions *via* the halogen atoms, consistent with the Goodenough–Kanamori–Anderson rules.

2. Computational methods

Spin-polarized first-principles calculations were performed within the density functional theory (DFT) framework, as implemented in the Quantum Espresso package.[42] The core electrons were treated within the projector augmented wave (PAW) method.[43] Exchange–correlation effects were described through the generalized gradient approximation (GGA) and the PBEsol exchange–correlation functional.[44] PBEsol is a revision of the PBE functional, specifically tailored for solids, and has been shown to produce better agreement with experimental data.[44] For accurate electronic structure prediction, we used the HSE06 hybrid functional including 25% non-local Hartree–Fock exchange.[45] The total energy of monolayers was calculated using a Γ-centered $15 \times 15 \times 1$ Monkhorst–Pack k-point grid for a primitive cell. The plane-wave cutoff is 50 Ryd (680 eV). Test calculations with a larger number of k points and higher cutoff energies produced the same results. The optimized structures were obtained by relaxing all atomic positions and lattice parameters using the Broyden–Fletcher–Goldfarb–Shanno (BFGS) quasi-Newton algorithm until all forces are smaller than 0.01 eV Å^{-1}. To account for the on-site Coulomb interactions between the 3d electrons, we performed DFT+U calculations by adding an effective parameter, U_{eff}.[46] We have used U_{eff} values for transition metals suggested by Ceder *et al.*[47] We have also performed additional tests using other U_{eff} values from 1.0 to 6.0 eV, and found that the use of different U_{eff} values leads to qualitatively similar results.

3. Results and discussion

3.1. Crystal structure and stability

First, we examine the atomic structure of dihalides MX_2 (M = V, Cr, Mn, Fe, Co, Ni, and X = Cl, Br, I). As shown by experimental studies, bulk metal dihalides have a natural layered structure as shown in Fig. 1a. Therefore, similar to graphene and MoS_2, individual layers of dihalides can be potentially extracted from the bulk using exfoliation techniques. For each monolayer, we have determined the minimum-energy structure by optimizing all atomic positions and lattice constants. The typical crystal structure of single-layer MX_2 is shown in Fig. 1b and c. The atomic geometry of monolayer dihalides is conceptually similar to the well-known transition-metal dichalcogenides (TMDCs). Namely, each metal dihalide is composed of three atomic planes: a layer of transition-metal (TM) atoms sandwiched between two layers of halogen atoms. Interestingly,
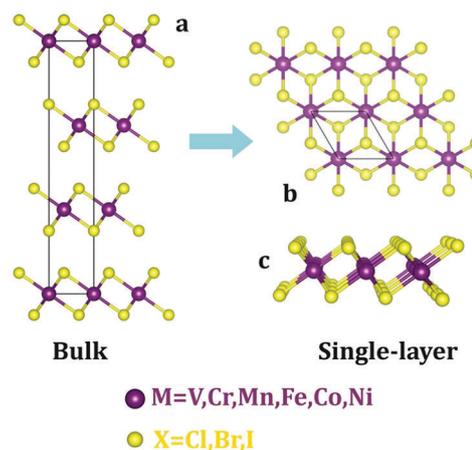

Fig. 1 Crystal structures of metal dihalides (MX_2) in the 1-T phase: (a) bulk and (b and c) single-layer. Top (b) and side (c) views are shown.

we find that all studied single-layer dihalides prefer the 1-T crystal structure (C_{3v} symmetry). Each metal atom is surrounded by 6 neighboring halogen atoms forming an octahedral $[MX_6]^{4-}$ unit. The 1-T crystal phase is also found in NbS_2 and $TiSe_2$, in contrast to the H phase in MoS_2 and WSe_2.[48] To assess the possibility of T–H phase transition, we computed the energy difference between these phases ($E = E_H - E_T$) for each monolayer (Fig. 2). We find that all relative energies are positive, indicating that 1-T is a ground-state structure. The energy associated with the T–H transition is considerable: several tenths of an eV per MX_2 formula unit. The computed absolute values are comparable to those in dichalcogenides, such as MoS_2, WSe_2 and VS_2.[48,49] The smallest H–T energy difference is found in Fe dihalides and the largest in V and Ni dihalides.

The calculated structural parameters of MX_2 are summarized in Table 1. The obtained lattice constants are in good agreement with experimental data on bulk structures.[50,51] The M–X bond lengths increase as M changes from V to Mn and then decrease to Ni. Both lattice parameters and M–X bond lengths increase with the element number of X (Cl → Br → I). These trends are consistent with the variations of the radii of the TM atoms in their +2 valence states, as well as increasing the atomic radius of halogen. All M–X–M bond angles are $\sim 90°$. The stability of single-layer dihalides can be evaluated from their formation

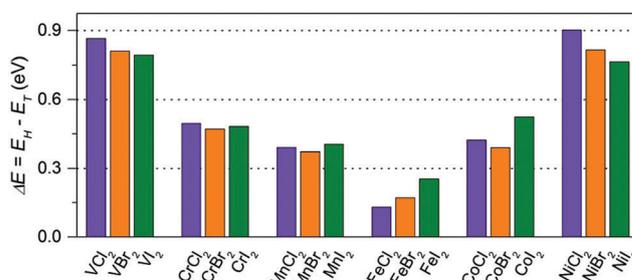**Fig. 2** The energy difference (per MX_2 formula unit) between H and T phases for all studied monolayers. The energies are computed at the equilibrium lattice parameters for each phase.

Table 1 Calculated structural parameters of single-layer MX_2 dihalides (X = Cl, Br, I): formation energy (E_{form}, in eV), theoretical lattice parameter ($a = b$, in Å), experimental lattice parameter ($a = b$, in Å), M–X bond length (d_{M-X}, in Å), and in-plane stiffness (C, in N m^{-1})

	E_{form}	a (DFT)	a (Exp.)	d_{M-X}	C
VCl_2	−3.46	3.58	3.60	2.45	25.63
VBr_2	−2.77	3.76	3.77	2.60	26.32
VI_2	−1.93	4.04	4.06	2.80	30.86
$CrCl_2$	−2.57	3.55	3.59	2.49	26.15
$CrBr_2$	−2.00	3.74	3.81	2.61	24.95
CrI_2	−1.28	3.99	4.08	2.81	22.01
$MnCl_2$	−3.23	3.64	3.68	2.51	33.08
$MnBr_2$	−2.65	3.80	3.82	2.66	29.77
MnI_2	−1.83	4.06	4.16	2.86	28.73
$FeCl_2$	−2.22	3.43	3.57	2.42	41.49
$FeBr_2$	−1.61	3.63	3.74	2.57	39.41
FeI_2	−0.83	3.91	4.04	2.77	37.92
$CoCl_2$	−1.71	3.42	3.54	2.38	20.19
$CoBr_2$	−1.15	3.62	3.68	2.53	21.74
CoI_2	−0.67	3.80	3.96	2.62	27.14
$NiCl_2$	−1.98	3.42	3.48	2.36	53.30
$NiBr_2$	−1.50	3.61	3.70	2.50	49.42
NiI_2	−0.96	3.88	3.89	2.69	46.64

energy as $E_{form} = E(MX_2) - \mu_M - 2\mu_X$. Here, μ_M and μ_X correspond to the energy per atom of the stable bulk (bcc-V, bcc-Cr, bcc-Mn, bcc-Fe, hcp-Co, fcc-Ni) and gas (Cl_2, Br_2, I_2) phases, respectively. We found that all calculated formation energies are negative in the range from −0.83 to −4.66 eV per M atom. These values are very close to the calculated formation energies of MoS_2, VS_2 and WSe_2 (−2.49, −2.79 and 1.86 eV per M atom, respectively).[48] Therefore, metal halide monolayers are energetically stable and could be potentially obtained by exfoliation.

To access the dynamical stability of single-layer dihalides, we calculated their phonon band structure using density functional perturbation theory (DFPT). The force constants were calculated for a 4 × 4 × 1 supercell by using Phonopy package.[52] Fig. S1 in the ESI† shows the phonon dispersions of all monolayers. We observe no imaginary (negative) frequencies, confirming the dynamical stability of single-layer dihalides.

We then determine the mechanical properties of halide monolayers by calculating their in-plane stiffness – the analogue of Young's modulus for 2D materials. This can be done by applying a series of small deformations on the material and monitoring its mechanical response. Starting with the fully relaxed structure of MX_2, its lattice constants are imposed to small strains ε_x and ε_y within the harmonic range of ±0.02. For each (ε_x, ε_y) pair, we fully optimize the structure and calculate the strain energy E_s. In the harmonic regime, the strain energy can be fitted to a two-dimensional quadratic polynomial expressed by

$$E_s(\varepsilon_x, \varepsilon_y) = a_1\varepsilon_x^2 + a_2\varepsilon_y^2 + a_3\varepsilon_x\varepsilon_y \tag{1}$$

Through fitting of the strain-energy surface, we can derive the in-plane stiffness (C) of single-layer dihalides as follows

$$C_x = \frac{4a_1a_2 - a_3^2}{2a_2A_0} \text{ and } C_y = \frac{4a_1a_2 - a_3^2}{2a_1A_0} \tag{2}$$

Here, A_0 is the equilibrium area of single-layer MX_2 in the orthorhombic cell. Table 1 summarizes the obtained results ($C = C_x = C_y$). The calculated in-plane stiffness of metal dihalides ranges from 20.19 to 53.30 N m^{-1}, which is comparable to those of germanene (48 N m^{-1}), phosphorene (30–94 N m^{-1}), arsenene (58 N m^{-1}), $CrSnTe_3$ (60 N m^{-1}), and $MnPSe_3$ (36 N m^{-1}) monolayers.[6,53–56] The single-layer dihalides demonstrate high flexibility with their in-plane stiffness being smaller than that of TMDCs, such as MoS_2 (140 N m^{-1}) and WSe_2 (130 N m^{-1}).[48] This may be attributed to the weaker ionic bonds in dihalides as compared to covalent bonds in TMDCs.

3.2. Electronic properties

Our spin-polarized calculations demonstrate that most transition-metal (TM) dihalides possess a large magnetic moment. The total magnetic moment forms a "volcano" curve (Fig. 3a) starting with V-halides (3 μ_B per TM atom), increasing to Mn-halides (5 μ_B), and then gradually decreasing to 2 μ_B for Ni-halides, in good agreement with the magnetic moments of free metal atoms, described by Hund's rules. The calculated magnetic moments in 2D dihalides are higher than those in magnetic 2D dichalcogenides (e.g. VS_2, NbS_2).[5,15,57] The majority of the total magnetic moment
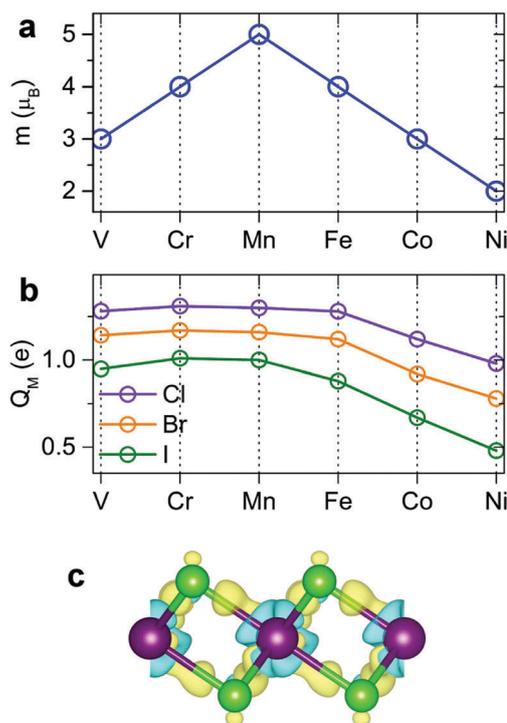

Fig. 3 Calculated magnetic and electronic properties of dihalide monolayers: (a) total magnetic moments per M atom, (b) Bader charges on M atoms, (c) charge density difference isosurface plot, showing charge accumulation and depletion (yellow and blue colors, respectively).

8736 | J. Mater. Chem. C, 2017, 5, 8734–8741

This journal is © The Royal Society of Chemistry 2017

comes from the TM atoms, while the halogens have a small magnetic moment of only 0.16–0.40 μ_B. The detailed analysis indicates that the local magnetic moment on TM atoms increases with the atomic number of the X atom (Cl → Br → I). This trend is opposite to the amount of electron transfer between TM and X atoms. The Cl atom has the largest electronegativity and withdraws the most valence electron charge from TM atoms, decreasing their magnetization.

The bonding mechanism is examined by plotting the electron density distribution. The distinctive feature of 2D metal halides is a significant charge transfer. The bonding has a profound ionic character. Halogen atoms have strong affinity for acquiring an extra electron to fill its outer shell, and the Bader charge analysis shows that 0.48–0.65 e is transferred from M to each Cl, 0.39–0.58 e from M to each Br, and 0.24–0.50 e from M to each I atom (Fig. 3b). The direction of charge transfer can be rationalized by much larger electronegativity of Cl, Br and I atoms *versus* metal atoms. The amount of charge transfer decreases going as Cl → Br → I. The charge distribution in dihalides was visualized by calculating the charge density difference ($\Delta\rho$) plots as shown in Fig. 3c. Here, $\Delta\rho$ is obtained as the difference between the charge density of the MX_2 monolayer and the superposition of the charge densities of the constituent atoms. The blue and yellow isosurfaces represent charge depletion and accumulation regions, respectively. There is noticeable electron depletion in the region of M atoms, consistent with electron affinities and Bader analysis.

We compare the densities of states (DOSs) calculated using GGA, GGA+U and HSE methods on the example of $NiCl_2$.

The GGA spin-polarized DOS of monolayer $NiCl_2$ is shown in Fig. 4a. The electronic structures of different dihalides share several common features. The valence band is formed by halogen p bands, while the bottom of the conduction band mainly originates from metal s states. The TM atoms transfer their 4s electrons to halogens and have a +2 oxidation state; therefore, TM 4s states are completely unoccupied. The spin-polarized 3d states of TM atoms are located within the band gap. We can observe significant hybridization between TM 3d and halogen p orbitals. Each TM atom is surrounded by six halogen neighbors ("ligands") which form a nearly spherical octahedral coordination. The octahedral crystal field splits the 3d orbitals of TM atoms into upper e_g ($d_{x^2-y^2}$, d_{z^2}) and lower t_{2g} (d_{xy}, d_{xz}, d_{yz}) states. The e_g orbitals point directly at the six negatively charged halogens, which increases their energy due to the electrostatic repulsion with halogens. In contrast, t_{2g} orbitals lie between the halogens, making them relatively more stable and lowering their energy. Halogens are weak ligands from the spectroscopic series; therefore, 3d TM atoms in the octahedral field are expected to prefer the high spin state. This is consistent with the large exchange splitting of the TM 3d states, as observed in Fig. 4.

The addition of on-site Coulomb repulsion (GGA+U, Fig. 4b and c) increases the exchange splitting between filled and empty orbitals in the TM 3d manifold. Consequently, the occupied spin-up TM 3d states now move towards the valence band and hybridize more strongly with the halogen p states. The unoccupied spin-down TM 3d states shift towards the CBM. GGA+U reduces the width of the TM 3d peak inside the
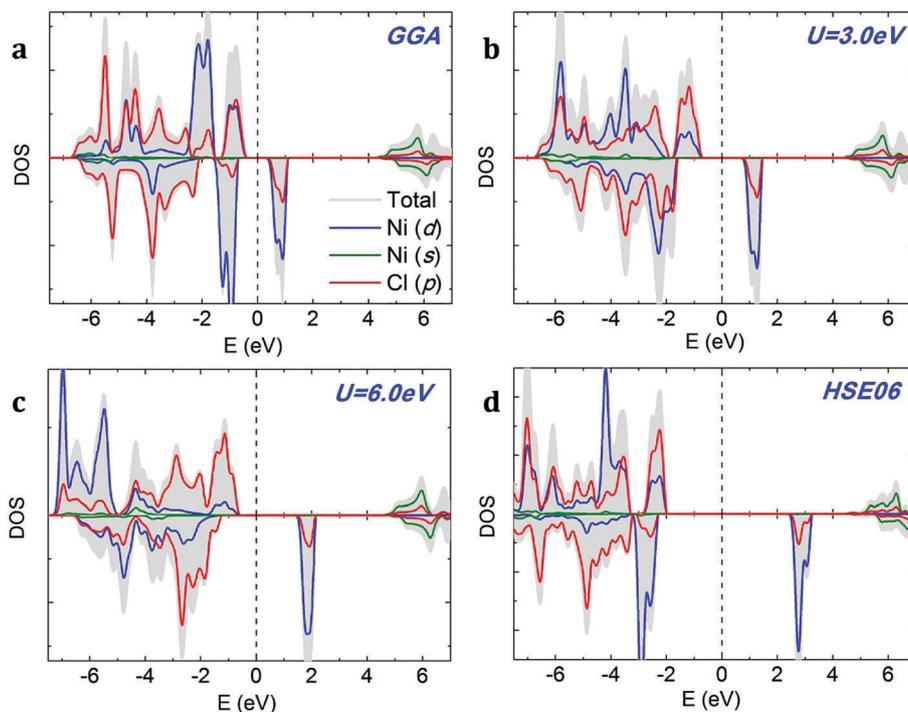

Fig. 4 Density of states (DOS) of monolayer $NiCl_2$ calculated using (a) GGA, (b and c) GGA+U, and (d) HSE06 methods. The Fermi level is indicated by a dashed vertical line.

band gap, suggesting stronger localization. As shown in Fig. 4c, the above-mentioned effects become even more pronounced as the on-site Coulomb repulsion (U_{eff}) increases from 3.0 to 6.0 eV. The DOS calculated using the high-accuracy HSE06 functional (Fig. 4d) confirms that $NiCl_2$ is a semiconductor. In agreement with GGA/GGA+U calculations, the VBM is formed by halogen p bands and the CBM originates from metal s states. There is a single spin-polarized peak in the middle of the band gap, formed by metal 3d states.

3.3. Magnetic ordering

The next step is to identify the preferable magnetic ordering in 2D dihalides. We have constructed a larger (2×2) supercell, and set the spin ordering to either ferromagnetic (FM) or antiferromagnetic (AFM), as shown in Fig. 5a. The exchange energy (E_{ex}) is calculated as $E_{ex} = E_{AFM} - E_{FM}$. Positive exchange energy indicates that the ground state of the system is ferromagnetic. From our calculations, we have found that FeX_2, CoX_2 and NiX_2 prefer the FM ground state, while VX_2, CrX_2 and MnX_2 are AFM. The observed preference for either FM or AFM ordering can be rationalized using the Goodenough–Kanamori–Anderson (GKA) formalism.[58–60] The magnetic properties of single-layer dihalides are governed by the competition between two distinct mechanisms (Fig. 5b): (i) the direct exchange between two TM atoms, and (ii) the halogen-mediated M–X–M superexchange interaction. In Mn dihalides, the direct exchange is robustly AFM as the Mn ions are in the half-filled high-spin d^5 state. In contrast, for the Fe, Co and Ni dihalides, the AFM direct exchange is weakened by a FM component as these ions have a nearly filled d-shell.[61] The sign of M–X–M superexchange can be predicted from the local crystal symmetry (M–X–M bond angles) and d electron configurations of TM atoms. In 2D dihalides, all calculated metal-halogen-metal (M–X–M) bond angles are $\sim90°$. In such a case, the d-orbitals on neighboring TM atoms overlap different halogen-p orbitals (Fig. 6) and are, therefore, orthogonal to one another. According to the GKA rules, in systems with $90°$
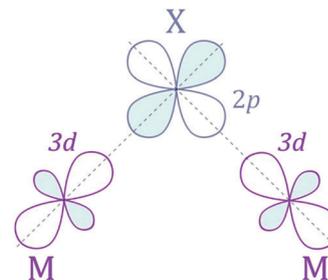

Fig. 6 Mechanism of M–X–M superexchange interaction for a $90°$ M–X–M bond angle.

bond angles the superexchange interaction between TM atoms is deduced only from a potential exchange which is always FM. The competition between FM and AFM components may lead to different magnetic states, depending on the TM atoms involved. For instance, Mn dihalides exhibit AFM properties because of the relatively large AFM direct exchange. However, in Fe, Co and Ni dihalides, the FM superexchange is dominating leading to the FM ground state. Overall, the 1-T crystal structure of Fe, Co and Ni dihalides containing $90°$ M–X–M bond angles represents a promising platform for stable and robust ferromagnetism.

3.4. Curie temperature

One of the critical properties of ferromagnetic materials is the Curie temperature (T_C) of a FM–AFM transition. It is possible to estimate T_C from the mean-field theory (MFT); however, such a value is often overestimated.[62] The more accurate prediction can be made using statistical Monte Carlo (MC) simulations based on the Ising model. This method has been successfully used to predict the T_C in other 2D materials producing values close to the experimental data.[6] Consider a set of magnetic spins located at the sites on a regular lattice of 2D halides. Neighboring spins interact though an exchange constant J. The system is described by the classical Heisenberg Hamiltonian:

$$H = -\sum_{i,j} J_{ij} S_i^z S_j^z \qquad (3)$$

where J_{ij} is the exchange coupling constant between i and j sites, S_i^z and S_j^z are spins parallel or antiparallel to the z direction. The exchange constant J is defined from the exchange energy as

$$J = \frac{E_{ex}}{2z S_{TM}^2} \qquad (4)$$

where $E_{ex} = E_{AFM} - E_{FM}$ is the exchange energy per TM atom, z is the number of nearest TM neighbors ($z = 6$ for single-layer dihalides), and S_{TM} is the spin of each TM atom. Here, the TM atoms are in high spin, octahedral configuration giving S_{TM} values of 3/2, 2, 5/2, 2, 3/2, and 1 for V, Cr, Mn, Fe, Co, and Ni, respectively. According to the above definition, $J > 0$ indicates FM coupling and $J < 0$ – AFM. Our calculated exchange constants for all dihalides are summarized in Table 2.

Within the MC scheme, the magnetic system goes through a number of spin configurations with a probability of "spin flip" that depends exponentially on the change in energy as a result
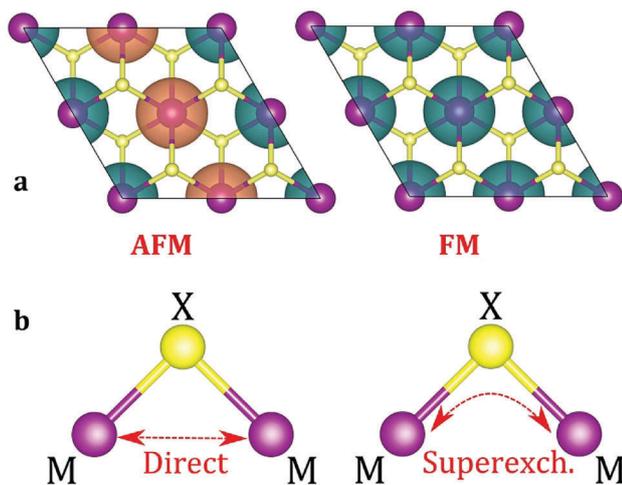

Fig. 5 (a) Spin density isosurface plots for AFM and FM spin arrangements. (b) Schematic mechanism of direct (M–M) and superexchange (M–X–M) interactions.

8738 | J. Mater. Chem. C, 2017, 5, 8734–8741

This journal is © The Royal Society of Chemistry 2017

Table 2 Calculated magnetic properties of single-layer MX_2 dihalides (X = Cl, Br, I): exchange energy per M atom ($E_{ex} = E(AFM) − E(FM)$, in meV), exchange constant (J, in meV), Curie temperature of FM to AFM transition from MC simulations (T_C^{MC}, in K), ground magnetic state (MS, at $T = 0$ K), and average magnetic moment per M atom (m, in units of the Bohr magneton μ_B)

	E_{ex}	J	T_C^{MC}	MS	m
VCl_2	−81.80	−3.03	—	AFM	3.0
VBr_2	−41.25	−1.53	—	AFM	3.0
VI_2	−14.85	−0.55	—	AFM	3.0
$CrCl_2$	−63.30	−1.32	—	AFM	4.0
$CrBr_2$	−32.09	−0.67	—	AFM	4.0
CrI_2			—	AFM	4.0
$MnCl_2$	−18.63	−0.25	—	AFM	5.0
$MnBr_2$	−15.65	−0.21	—	AFM	5.0
MnI_2	−15.43	−0.21	—	AFM	5.0
$FeCl_2$	122.58	2.55	109	FM	4.0
$FeBr_2$	90.05	1.88	81	FM	4.0
FeI_2	47.48	0.99	42	FM	4.0
$CoCl_2$	53.05	1.96	85	FM	3.0
$CoBr_2$	14.35	0.53	23	FM	3.0
CoI_2	−12.83	−0.48	—	AFM	3.0
$NiCl_2$	38.55	3.21	138	FM	2.0
$NiBr_2$	37.33	3.11	132	FM	2.0
NiI_2	36.28	3.02	129	FM	2.0

of the flip. We use a Metropolis algorithm and a 100×100 two-dimensional supercell with periodic boundary conditions. The MC simulation is run for 10^6 steps. Fig. 7a shows the calculated magnetization per TM atom as a function of temperature. At low temperatures, all spins are aligned parallel, producing a large net magnetic moment (FM state). At high temperatures, the spins are aligned randomly resulting in zero net magnetization (AFM state). The calculated Curie temperatures of FM/AFM phase transitions are summarized in Table 2. The calculated T_C values are comparable with those in the state-of-the-art 2D magnetic materials, such as $CrSiTe_3$ (36–90 K), $CrGeTe_3$ (57–130 K) and $CrSnTe_3$ (170 K).[6,63] The T_C values for all dihalides are decreasing from Cl to Br to I, consistent with the trends in exchange energies. Remarkably, single-layer dihalides exhibit comparable or even slightly higher Curie temperatures than single-layer dichalcogenides (for example, 90 K in VS_2).[57] This can be attributed to the profound ionic bonding in halides, which enhances the superexchange coupling between the magnetic metal ions *via* halogen p states, consistent with the GKA rules.[6]

The Curie temperature can be further increased by applying strain and/or carrier doping.[7,15,64–70] The outstanding elastic behaviour and stretchability of 2D crystals can potentially lead to novel tunability levels which are not accessible in conventional bulk semiconductors. For example, MoS_2 can sustain in-plane strain levels as large as 11% and has a high Young's modulus of $\sim$270 GPa.[71] In contrast, bulk silicon can be strained to only $\sim$1.5% before breaking.[72] On the other hand, hole doping has been shown to promote ferromagnetism and half-metallicity in single-layer materials, such as GaSe, CrI_3 and phosphorene.[27,40,73,74] Taking $FeCl_2$ as a prototype, we first apply
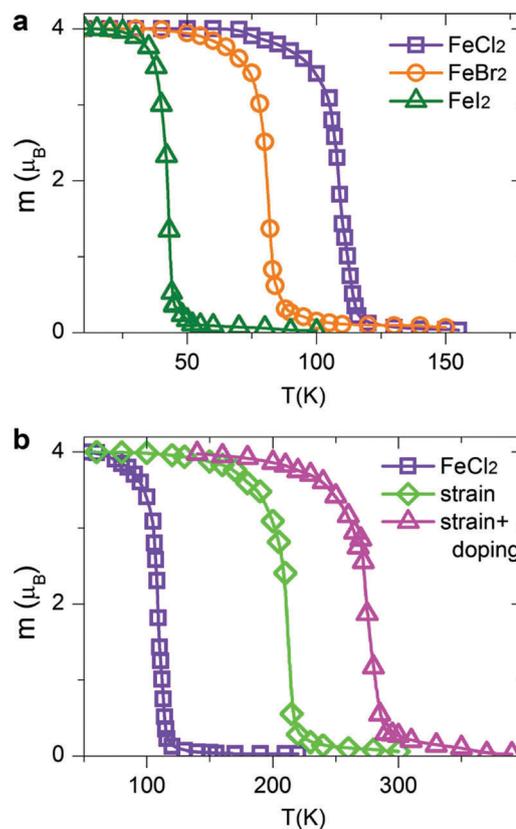
Fig. 7 Variation of the calculated magnetization per TM atom *versus* temperature for (a) pristine $FeCl_2$, $FeBr_2$ and FeI_2, and (b) strained and hole-doped $FeCl_2$ monolayers.

biaxial in-plane strain ranging from −10% to +10%. To simulate the effect of carrier doping, we add/remove electrons from $FeCl_2$ and use a compensating jellium background to maintain charge neutrality. Note that high doping carrier densities of up to 10^{14} cm^{-2} have been achieved by electrostatic gating in graphene and MoS_2.[75,76] We therefore expect that hole doping levels, described in this work, are experimentally feasible. Remarkably, we find that both biaxial strain and carrier doping can enhance the magnetic properties of $FeCl_2$. At a strain level of 10%, the calculated exchange energy increases from 122.57 meV per unit cell in pristine $FeCl_2$ to 234.52 meV in the strained one. It is possible to further increase the exchange energy to 307.85 meV using a combination of strain and carrier doping. Fig. 7b shows the magnetization *versus* temperature for pristine, stained and hole-doped $FeCl_2$. The corresponding Curie temperatures are found to be 109, 212 and 273 K, respectively, suggesting a high degree of tunability and promising potential of single-layer dihalides for room-temperature spintronic devices.

4. Conclusions

In summary, we have investigated the structural, electronic and magnetic properties of single-layer metal dihalides using first-principles calculations with the GGA, GGA+U and hybrid HSE06 functionals. We found that single-layer dihalides prefer the 1-T

This journal is © The Royal Society of Chemistry 2017

J. Mater. Chem. C, 2017, **5**, 8734–8741 | **8739**

crystal phase and are energetically stable. The magnetic properties of 2D dihalides are governed by the competition between AFM direct nearest-neighbor d–d exchange and FM superexchange *via* halogen p states, which leads to different magnetic states. Thus we found that 2D FeX_2, NiX_2, $CoCl_2$ and $CoBr_2$ monolayers are ferromagnetic (FM), while VX_2, CrX_2 and MnX_2 are antiferromagnetic (AFM). Using the DFT derived spin exchange parameters, we estimated the Curie temperature of magnetic transition from the Monte Carlo simulations based on the Ising model and Heisenberg Hamiltonian. We find that single-layer dihalides exhibit comparable or even slightly higher Curie temperatures than single-layer dichalcogenides. This can be attributed to the profound ionic bonding in halides, which enhances the superexchange coupling between the magnetic metal ions *via* the halogen atoms. Overall, single-layer dihalides represent a new addition to the family of 2D materials with promising applications in nanoscale devices. We expect that our theoretical results will inspire further experimental studies.

Acknowledgements

References

1 K. F. Mak and J. Shan, *Nat. Photonics*, 2016, **10**, 216–226.
2 L. Shi and T. S. Zhao, *J. Mater. Chem. A*, 2017, **5**, 3735–3758.
3 B. Luo, G. Liu and L. Wang, *Nanoscale*, 2016, **8**, 6904–6920.
4 W. Han, R. K. Kawakami, M. Gmitra and J. Fabian, *Nat. Nanotechnol.*, 2014, **9**, 794–807.
5 Y. Ma, Y. Dai and M. Guo, *et al.*, *ACS Nano*, 2012, **6**, 1695–1701.
6 H. L. Zhuang, Y. Xie, P. R. C. Kent and P. Ganesh, *Phys. Rev. B: Condens. Matter Mater. Phys.*, 2015, **92**, 035407.
7 Y. Wang, S.-S. Wang, Y. Lu, J. Jiang and S. A. Yang, *Nano Lett.*, 2016, **16**, 4576–4582.
8 L. Hu, X. Wu and J. Yang, *Nanoscale*, 2016, **8**, 12939–12945.
9 H. L. Zhuang, P. R. C. Kent and R. G. Hennig, *Phys. Rev. B*, 2016, **93**, 134407.
10 H. Y. Lv, W. J. Lu, D. F. Shao, Y. Liu and Y. P. Sun, *Phys. Rev. B: Condens. Matter Mater. Phys.*, 2015, **92**, 214419.
11 J. Liu, Z. Liu, T. Song and X. Cui, *J. Mater. Chem. C*, 2017, **5**, 727–732.
12 Y. Sun, Z. Zhuo, X. Wu and J. Yang, *Nano Lett.*, 2017, **17**, 2771–2777.
13 E. Kan, W. Hu and C. Xiao, *et al.*, *J. Am. Chem. Soc.*, 2012, **134**, 5718–5721.
14 H. Wang, J. Zhang and X. Hang, *et al.*, *Angew. Chem., Int. Ed.*, 2015, **54**, 1195–1199.
15 Y. Zhou, Z. Wang and P. Yang, *et al.*, *ACS Nano*, 2012, **6**, 9727–9736.
16 E. J. Duplock, M. Scheffler and P. J. D. Lindan, *Phys. Rev. Lett.*, 2004, **92**, 225502.
17 O. V. Yazyev and L. Helm, *Phys. Rev. B: Condens. Matter Mater. Phys.*, 2007, **75**, 125408.
18 V. V. Kulish, O. I. Malyi, C. Persson and P. Wu, *Phys. Chem. Chem. Phys.*, 2015, **17**, 992–1000.
19 V. V. Kulish, *Phys. Chem. Chem. Phys.*, 2017, **19**, 11273–11281.
20 H. Sevincli, M. Topsakal, E. Durgun and S. Ciraci, *Phys. Rev. B: Condens. Matter Mater. Phys.*, 2008, **77**, 195434.
21 Z. Li, W. Xu and Y. Yu, *et al.*, *J. Mater. Chem. C*, 2016, **4**, 362–370.
22 B. Onat, L. Hallioglu, S. pek and E. Durgun, *J. Phys. Chem. C*, 2017, **121**, 4583–4592.
23 M. Sun, Q. Ren and Y. Zhao, *et al.*, *Carbon*, 2017, **120**, 265–273.
24 M. Sun, Q. Ren and Y. Zhao, *et al.*, *J. Appl. Phys.*, 2016, **119**, 143904.
25 W.-B. Zhang, Q. Qu, P. Zhu and C.-H. Lam, *J. Mater. Chem. C*, 2015, **3**, 12457–12468.
26 Y. Zhou, H. Lu, X. Zu and F. Gao, *Sci. Rep.*, 2016, **6**, 19407.
27 J. Liu, Q. Sun, Y. Kawazoe and P. Jena, *Phys. Chem. Chem. Phys.*, 2016, **18**, 8777–8784.
28 J. He, S. Ma, P. Lyu and P. Nachtigall, *J. Mater. Chem. C*, 2016, **4**, 2518–2526.
29 R. E. Brandt, R. C. Kurchin and R. L. Z. Hoye, *et al.*, *J. Phys. Chem. Lett.*, 2015, **6**, 4297–4302.
30 A. J. Lehner, H. Wang and D. H. Fabini, *et al.*, *Appl. Phys. Lett.*, 2015, **107**, 131109.
31 F. Ma, M. Zhou and Y. Jiao, *et al.*, *Sci. Rep.*, 2015, **5**, 17558.
32 A. J. Lehner, D. H. Fabini and H. A. Evans, *et al.*, *Chem. Mater.*, 2015, **27**, 7137–7148.
33 M. Zhou, W. Duan, Y. Chen and A. Du, *Nanoscale*, 2015, **7**, 15168–15174.
34 A. S. Toulouse, B. P. Isaacoff and G. Shi, *et al.*, *Phys. Rev. B: Condens. Matter Mater. Phys.*, 2015, **91**, 165308.
35 L. Li, O. Leenaerts and X. Kong, *et al.*, *Nano Res.*, 2017, **10**, 2168–2180.
36 L. Zhou, L. Kou and Y. Sun, *et al.*, *Nano Lett.*, 2015, **15**, 7867–7872.
37 E. Torun, H. Sahin, S. K. Singh and F. M. Peeters, *Appl. Phys. Lett.*, 2015, **106**, 192404.
38 E. Torun, H. Sahin, C. Bacaksiz, R. T. Senger and F. M. Peeters, *Phys. Rev. B: Condens. Matter Mater. Phys.*, 2015, **92**, 104407.
39 M. A. McGuire, H. Dixit, V. R. Cooper and B. C. Sales, *Chem. Mater.*, 2015, **27**, 612–620.
40 W. Hongbo, F. Fengren, Z. Shasha and W. Hua, *EPL*, 2016, **114**, 47001.
41 B. Huang, G. Clark and E. Navarro-Moratalla, *et al.*, *Nature*, 2017, **546**, 270–273.
42 P. Giannozzi, S. Baroni and N. Bonini, *et al.*, *J. Phys.: Condens. Matter*, 2009, **21**, 19.
43 P. E. Blochl, *Phys. Rev. B: Condens. Matter Mater. Phys.*, 1994, **50**, 17953–17979.
44 J. P. Perdew, A. Ruzsinszky and G. I. Csonka, *et al.*, *Phys. Rev. Lett.*, 2008, **100**, 136406.
45 J. Heyd, G. E. Scuseria and M. Ernzerhof, *J. Chem. Phys.*, 2003, **118**, 8207–8215.

46 V. I. Anisimov, F. Aryasetiawan and A. I. Lichtenstein, *J. Phys.: Condens. Matter*, 1997, **9**, 767–808.

47 L. Wang, T. Maxisch and G. Ceder, *Phys. Rev. B: Condens. Matter Mater. Phys.*, 2006, **73**, 195107.

48 C. Ataca, H. Sahin and S. Ciraci, *J. Phys. Chem. C*, 2012, **116**, 8983–8999.

49 K.-A. N. Duerloo, Y. Li and E. J. Reed, *Nat. Commun.*, 2014, **5**, 4214.

50 R. W. G. Wyckoff, *Crystal structures*, Interscience Publishers, New York, 1963.

51 S. R. Kuindersma, C. Haas, J. P. Sanchez and R. Al, *Solid State Commun.*, 1979, **30**, 403–408.

52 A. Togo and I. Tanaka, *Scr. Mater.*, 2015, **108**, 1–5.

53 H. Sahin, S. Cahangirov and M. Topsakal, *et al.*, *Phys. Rev. B: Condens. Matter Mater. Phys.*, 2009, **80**, 155453.

54 V. V. Kulish, O. I. Malyi, C. Persson and P. Wu, *Phys. Chem. Chem. Phys.*, 2015, **17**, 13921–13928.

55 X. Li, X. Wu and J. Yang, *J. Am. Chem. Soc.*, 2014, **136**, 11065–11069.

56 D. Kecik, E. Durgun and S. Ciraci, *Phys. Rev. B*, 2016, **94**, 205409.

57 H. L. Zhuang and R. G. Hennig, *Phys. Rev. B*, 2016, **93**, 054429.

58 J. B. Goodenough, *Phys. Rev.*, 1955, **100**, 564–573.

59 J. Kanamori, *J. Appl. Phys.*, 1960, **31**, S14–S23.

60 P. W. Anderson, *Phys. Rev.*, 1959, **115**, 2–13.

61 N. Sivadas, M. W. Daniels, R. H. Swendsen, S. Okamoto and D. Xiao, *Phys. Rev. B: Condens. Matter Mater. Phys.*, 2015, **91**, 235425.

62 N. W. Ashcroft and N. D. Mermin, *Solid State Physics*, Holt, Rinehart and Winston, 1976.

63 X. Li and J. Yang, *J. Mater. Chem. C*, 2014, **2**, 7071–7076.

64 R. Roldán, A. Castellanos-Gomez, E. Cappelluti and F. Guinea, *J. Phys.: Condens. Matter*, 2015, **27**, 313201.

65 S. Manzeli, A. Allain, A. Ghadimi and A. Kis, *Nano Lett.*, 2015, **15**, 5330–5335.

66 A. S. Rodin, A. Carvalho and A. H. Castro Neto, *Phys. Rev. Lett.*, 2014, **112**, 176801.

67 A. Castellanos-Gomez, R. Roldán and E. Cappelluti, *et al.*, *Nano Lett.*, 2013, **13**, 5361–5366.

68 L. C. Gomes, A. Carvalho and A. C. Neto, *Phys. Rev. B: Condens. Matter Mater. Phys.*, 2015, **92**, 214103.

69 S. Guan, Y. Cheng and C. Liu, *et al.*, *Appl. Phys. Lett.*, 2015, **107**, 231904.

70 L. Zhu, S.-S. Wang and S. Guan, *et al.*, *Nano Lett.*, 2016, **16**, 6548–6554.

71 S. Bertolazzi, J. Brivio and A. Kis, *ACS Nano*, 2011, **5**, 9703–9709.

72 J. Munguia, G. Bremond, J. M. Bluet, J. M. Hartmann and M. Mermoux, *Appl. Phys. Lett.*, 2008, **93**, 102101.

73 T. Cao, Z. Li and S. G. Louie, *Phys. Rev. Lett.*, 2015, **114**, 236602.

74 B. Fu, W. Feng, X. Zhou and Y. Yao, *2D Mater.*, 2017, **4**, 025107.

75 J. Ye, M. F. Craciun and M. Koshino, *et al.*, *Proc. Natl. Acad. Sci. U. S. A.*, 2011, **108**, 13002–13006.

76 K. F. Mak, K. He and C. Lee, *et al.*, *Nat. Mater.*, 2013, **12**, 207–211.

This journal is © The Royal Society of Chemistry 2017

J. Mater. Chem. C, 2017, **5**, 8734–8741 | 8741